Three-dimensional shallow water system: A relaxation approach

Xin Liu [a,*], Abdolmajid Mohammadian [a], Julio Ángel Infante Sedano [a], Alexander Kurganov [b,c]

[a] *Department of Civil Engineering, University of Ottawa, Ottawa, ON K1N6N5, Canada*
[b] *Department of Mathematics, Southern University of Science and Technology of China, Shenzhen, 518055, China*
[c] *Mathematics Department, Tulane University, New Orleans, LA 70118, USA*

ARTICLE INFO

ABSTRACT

We study a three-dimensional shallow water system, which is obtained from the three-dimensional Navier–Stokes equations after Reynolds averaging and under the simplifying hydrostatic pressure assumption. Since the three-dimensional shallow water system is generically not hyperbolic, it cannot be numerically solved using hyperbolic shock capturing schemes. At the same time, existing simple finite-difference and finite-volume methods may fail in simulations of unsteady flows with sharp gradients, such as dam-break and flood flows. To overcome this limitation, we propose a novel numerical method, which is based on a relaxation approach utilized to "hyperbolize" the three-dimensional shallow water system. The extended relaxation system is hyperbolic and we develop a second-order semi-discrete central-upwind scheme for it. The proposed numerical method can preserve "lake at rest" steady states and positivity of water depth over irregular bottom topography. The accuracy, stability and robustness of the developed numerical method is verified on five numerical experiments.

© 2016 Elsevier Inc. All rights reserved.

1. Introduction

Two-dimensional (2-D) depth-averaged shallow water equations (SWEs) have been widely used in studying various hydrodynamic phenomena including dam-break flows, flood waves, and tidal flows among others. The popularity of the 2-D SWEs hinges on the following facts. First, they are substantially simpler than the three-dimensional (3-D) Navier–Stokes equations and thus can be more efficiently solved numerically. At the same time, the 2-D SWEs are capable of describing the main features of the water flow in regimes when the wave lengths are much larger than the water depth. Since the 2-D shallow water system is a hyperbolic system of balance laws, it can be accurately solved using the finite-volume methods, in particular, Godunov-type schemes, which are designed to capture both shocks and contact discontinuities. For applications of Godunov-type schemes to the 2-D SWEs, we refer the reader to, e.g., [3,4,10,16,22,25,29,34,40,50,56] and references therein.

A major drawback of the 2-D SWEs is that they are depth-averaged and thus do not take into account any vertical variation of the water flow. The 3-D shallow water system, proposed in [6,7], is still substantially simpler than the 3-D Navier–Stokes equations, and unlike the 2-D SWEs it can predict the vertical distribution of primitive variables, information

* Corresponding author.
  E-mail addresses: xliu111@uottawa.ca (X. Liu), majid.mohammadian@uottawa.ca (A. Mohammadian), jinfante@uottawa.ca (J.Á. Infante Sedano), kurganov@math.tulane.edu (A. Kurganov).

on which is essential in many practical cases. Therefore, the 3-D SWEs have recently attracted a lot of attention as a more accurate alternative to the 2-D SWEs; see, e.g., [2,9,12,13,17,24,33,35,36,44,51].

After Reynolds averaging and under the simplifying hydrostatic pressure assumption, the 3-D SWEs with constant density and free surface are derived from the 3-D Navier–Stokes equations. The governing equations have the following form [6,7]:

$$u_x + v_y + w_z = 0,$$
$$u_t + (uu)_x + (uv)_y + (uw)_z = -g\eta_x, \qquad (1)$$
$$v_t + (vu)_x + (vv)_y + (vw)_z = -g\eta_y,$$

where t is the time; x, y and z are the spatial coordinates; $u(x, y, z, t)$, $v(x, y, z, t)$ and $w(x, y, z, t)$ are the velocity components in the x-, y- and z-directions, respectively; g is the gravitational acceleration; and $\eta(x, y, t)$ is the water surface elevation. The system (1) together with either kinematic or dynamic boundary conditions for η constitute a closed system of equations for u, v, w and η.

In order to avoid the difficulties with applying the boundary conditions on the free surface and representing the irregular bottom, we follow the approach in [6,7,43] and replace the vertical coordinate z with the σ coordinate, which normalizes the vertical dimension to unity by the following transformation:

$$\sigma = \frac{z - \eta(x, y, t)}{D(x, y, t)},$$

in which σ is the transformed vertical coordinate that varies between -1 and 0, and $D(x, y, t)$ is the depth of the water column computed by

$$D(x, y, t) = \eta(x, y, t) - h(x, y),$$

where $h(x, y)$ is the bed level. Accordingly, the governing equations (1) can be written in the following form:

$$\eta_t + (Du)_x + (Dv)_y + \Omega_\sigma = 0, \qquad (2)$$
$$(Du)_t + \left(Du^2 + \frac{g}{2}D^2\right)_x + (Dvu)_y + (\Omega u)_\sigma = -gDh_x, \qquad (3)$$
$$(Dv)_t + (Dvu)_x + \left(Dv^2 + \frac{g}{2}D^2\right)_y + (\Omega v)_\sigma = -gDh_y, \qquad (4)$$

where Ω represents the vertical velocity in the σ-direction, which is related to w through

$$w = \Omega + u\left(\sigma D_x + \eta_x\right) + v\left(\sigma D_y + \eta_y\right) + \left(\sigma D_t + \eta_t\right).$$

To close the system (2)–(4), we apply the kinematic boundary conditions, namely, $\Omega(x, y, \sigma = -1, t) = 0$ and $\Omega(x, y, \sigma = 0, t) = 0$, and integrate equation (2) with respect to σ from -1 to 0 to obtain

$$\eta_t + \left[\int_{-1}^{0} Du \, d\sigma\right]_x + \left[\int_{-1}^{0} Dv \, d\sigma\right]_y = 0. \qquad (5)$$

Note that equation (2) is an elliptic equation for Ω, since using the same kinematic boundary conditions, one can rewrite equation (2) by integrating it with respect to the σ-coordinate as follows:

$$\Omega(x, y, \sigma, t) = -\int_{-1}^{\sigma} \left[\eta_t(x, y, t) + (Du)_x(x, y, \xi, t) + (Dv)_y(x, y, \xi, t)\right] d\xi. \qquad (6)$$

The 3-D shallow water system (2)–(5) has been intensively studied and several finite difference (see, e.g., [2,11,12,17,24, 33,35,36,44,51]) and finite-volume (see, e.g., [9,13]) methods for (2)–(5) have been developed. However, these methods are only applicable to smooth solutions, and thus they may fail when unsteady flows with sharp gradients such as dam-break and flood flows are simulated. This problem significantly limits the applicability of the 3-D SWEs in many problems of interest. To overcome this difficulty and extend the applicability of 3-D SWEs, one potential way is to develop shock-capturing methods for this model (this class of methods cannot be directly applied to the 3-D shallow water system, which is not hyperbolic). In order to address this issue, we propose a relaxation approach inspired by [14,47], where a hyperbolic model of compressible two-phase flow was developed using the pressure relaxation, and [1], where an unconditionally hyperbolic two-layer SWEs were obtained using the relaxation in two auxiliary layer depth variables. In §2, we present a relaxation model of the 3-D SWEs, which replaces the system (2)–(4) with the hyperbolic one that includes an additional equation on an auxiliary vertical velocity.

We then develop a second-order semi-discrete central-upwind scheme for the obtained relaxation system. Godunov-type central-upwind schemes were developed in [26,27,30,31] for general multidimensional hyperbolic systems. The central-upwind scheme was extended to the one-dimensional (1-D) SWEs in [25]. A more robust, well-balanced and at the same

time positivity preserving central-upwind scheme for the 1-D SWEs was developed in [29]. The central-upwind scheme for the 2-D SWEs was proposed using both Cartesian [25,29], triangular [10], cell-vertex [5] and unstructured quadrilateral [48] grids. These schemes are capable of exactly preserving "lake at rest" steady states and ensuring the positivity of the computed water depth. In this paper, we propose a new central-upwind scheme on 3-D prismatic grids and apply it to the relaxation model of the 3-D SWEs. Our method, presented in §3, includes a well-balanced discretization of the bed-slope source term, continuous piecewise linear approximation of the bottom topography and positivity preserving linear reconstruction of the water surface: as we show, this ensures both well-balanced and positivity preserving properties of the resulting scheme.

Finally, in §4, we present several numerical experiments, where the robustness and high accuracy of the proposed relax-ation approach and new central-upwind scheme on prismatic grids are illustrated. Some concluding remarks complete the paper in §5.

2. Relaxation model

In this section, we construct a relaxation model of the studied system, which is hyperbolic and equivalent to the original model in the zero relaxation limit. In §3, we take advantage of the hyperbolicity of the constructed relaxation model and numerically solve it using the central-upwind scheme.

In order to obtain the relaxation model, we introduce an auxiliary variable Ω' and add a PDE with a stiff source term to the original system, in which the variable Ω is replaced with Ω':

$$\eta_t + (Du)_x + (Dv)_y + \Omega'_\sigma = 0, \tag{7}$$

$$(Du)_t + \left(Du^2 + \frac{g}{2}D^2\right)_x + (Duv)_y + (\Omega'u)_\sigma = -gDh_x, \tag{8}$$

$$(Dv)_t + (Duv)_x + \left(Dv^2 + \frac{g}{2}D^2\right)_y + (\Omega'v)_\sigma = -gDh_y, \tag{9}$$

$$\Omega'_t + W^*\Omega'_\sigma = -\frac{1}{\varepsilon}(\Omega' - \Omega). \tag{10}$$

Here, $\varepsilon > 0$ is a relaxation parameter and W^* is a (very) small advection parameter associated with the auxiliary variable Ω'; see Remark 2.1 below.

The system (7)–(10) can be written in the following vector form:

$$\boldsymbol{U}_t + \boldsymbol{F}(\boldsymbol{U}, h)_x + \boldsymbol{G}(\boldsymbol{U}, h)_y + \boldsymbol{J}(\boldsymbol{U}, h)_\sigma = \boldsymbol{S}(\boldsymbol{U}, h) + \boldsymbol{R}(\boldsymbol{U}), \quad \boldsymbol{U} := \left(\eta, Du, Dv, \Omega'\right)^T, \tag{11}$$

where $\boldsymbol{F}$, $\boldsymbol{G}$ and $\boldsymbol{J}$ are the fluxes:

$$\begin{aligned}
\boldsymbol{F}(\boldsymbol{U}, h) &:= \left(Du, \frac{(Du)^2}{\eta - h} + \frac{g}{2}(\eta - h)^2, \frac{(Du)(Dv)}{\eta - h}, 0\right)^T, \\
\boldsymbol{G}(\boldsymbol{U}, h) &:= \left(Dv, \frac{(Du)(Dv)}{\eta - h}, \frac{(Dv)^2}{\eta - h} + \frac{g}{2}(\eta - h)^2, 0\right)^T, \\
\boldsymbol{J}(\boldsymbol{U}, h) &:= \left(\Omega', \frac{(Du)\Omega'}{\eta - h}, \frac{(Dv)\Omega'}{\eta - h}, W^*\Omega'\right)^T,
\end{aligned} \tag{12}$$

and $\boldsymbol{S}$ and $\boldsymbol{R}$ are the source terms:

$$\boldsymbol{S}(\boldsymbol{U}, h) := \left(0, -(\eta - h)gh_x, -(\eta - h)gh_y, 0\right)^T, \quad \boldsymbol{R}(\boldsymbol{U}) := \left(0, 0, 0, -\frac{1}{\varepsilon}(\Omega' - \Omega)\right)^T. \tag{13}$$

The relaxation system (7)–(10) can be also written in the following quasi-linear form:

$$\boldsymbol{U}_t + A(\boldsymbol{U}, h)\boldsymbol{U}_x + B(\boldsymbol{U}, h)\boldsymbol{U}_y + C(\boldsymbol{U}, h)\boldsymbol{U}_\sigma = \boldsymbol{S}(\boldsymbol{U}, h) + \boldsymbol{R}(\boldsymbol{U}),$$

where the Jacobians $A := \frac{\partial \boldsymbol{F}}{\partial \boldsymbol{U}}$, $B := \frac{\partial \boldsymbol{G}}{\partial \boldsymbol{U}}$ and $C := \frac{\partial \boldsymbol{J}}{\partial \boldsymbol{U}}$ are

$$A(\boldsymbol{U}, h) = \begin{pmatrix} 0 & 1 & 0 & 0 \\ -\frac{(Du)^2}{(\eta-h)^2} + g(\eta - h) & \frac{2Du}{\eta-h} & 0 & 0 \\ -\frac{(Du)(Dv)}{(\eta-h)^2} & \frac{Dv}{\eta-h} & \frac{Du}{\eta-h} & 0 \\ 0 & 0 & 0 & 0 \end{pmatrix},$$

$$B(\boldsymbol{U}, h) = \begin{pmatrix} 0 & 0 & 1 & 0 \\ -\dfrac{(Du)(Dv)}{(\eta-h)^2} & \dfrac{Dv}{\eta-h} & \dfrac{Du}{\eta-h} & 0 \\ -\dfrac{(Dv)^2}{(\eta-h)^2} + g(\eta-h) & 0 & \dfrac{2Dv}{\eta-h} & 0 \\ 0 & 0 & 0 & 0 \end{pmatrix},$$

and

$$C(\boldsymbol{U}, h) = \begin{pmatrix} 0 & 0 & 0 & 1 \\ -\dfrac{(Du)\Omega'}{(\eta-h)^2} & \dfrac{\Omega'}{\eta-h} & 0 & \dfrac{Du}{\eta-h} \\ -\dfrac{(Dv)\Omega'}{(\eta-h)^2} & 0 & \dfrac{\Omega'}{\eta-h} & \dfrac{Dv}{\eta-h} \\ 0 & 0 & 0 & W^* \end{pmatrix},$$

respectively. Their eigenvalues are given by

$$\mathrm{spec}(A(\boldsymbol{U}, h)) = \left\{ \frac{Du}{\eta-h} - \sqrt{g(\eta-h)}, \ \frac{Du}{\eta-h}, \ \frac{Du}{\eta-h} + \sqrt{g(\eta-h)}, \ 0 \right\},$$

$$\mathrm{spec}(B(\boldsymbol{U}, h)) = \left\{ \frac{Dv}{\eta-h} - \sqrt{g(\eta-h)}, \ \frac{Dv}{\eta-h}, \ \frac{Dv}{\eta-h} + \sqrt{g(\eta-h)}, \ 0 \right\},$$

and

$$\mathrm{spec}(C(\boldsymbol{U}, h)) = \left\{ \frac{\Omega'}{\eta-h}, \ \frac{\Omega'}{\eta-h}, \ 0, \ W^* \right\}.$$

Remark 2.1. We note that the use of large advection parameter W^* will affect the stability restriction on the size of time-step, which is inversely proportional to the spectral radii of the matrices $A(\boldsymbol{U}, h)$, $B(\boldsymbol{U}, h)$ and $C(\boldsymbol{U}, h)$. This is the reason why we suggest to use a value of W^*, which is smaller than $\|\frac{\Omega'}{\eta-h}\|_\infty$. In all of our numerical experiments, we have taken $W^* = 10^{-8}$ that has satisfied this requirement.

In the numerical method presented in the next section, we will solve the relaxation system (11)–(13) using an operator splitting approach: We first evolve the solution by solving the propagation system

$$\boldsymbol{U}_t + \boldsymbol{F}(\boldsymbol{U}, h)_x + \boldsymbol{G}(\boldsymbol{U}, h)_y + \boldsymbol{J}(\boldsymbol{U}, h)_\sigma = \boldsymbol{S}(\boldsymbol{U}, h), \tag{14}$$

and then update it according to the (infinitely) fast relaxation step $\boldsymbol{U}_t = \boldsymbol{R}(\boldsymbol{U})$ with very small ε (or even with $\varepsilon \to 0+$).

3. Numerical method

In this section, we present a numerical method for the 3-D SWEs. Notice that even though the system (7)–(10) is hyperbolic, one cannot solve it directly since the water surface variable η is independent of σ. We therefore proceed in the following four steps:

Step 1 (§3.1). The discharge components Du and Dv and the auxiliary variable Ω' are evolved by numerically solving equations (8)–(10) from a given time level $t = t^n$ to the next time level $t = t^{n+1} := t^n + \Delta t^n$. The evolved cell averages of Ω' are denoted by $(\overline{\Omega'_i})^*$ since they are to be corrected at Step 4;

Step 2 (§3.2). The water surface elevation η is then updated from the time level $t = t^n$ to $t = t^{n+1}$ by numerically solving the depth-averaged equation (5);

Step 3 (§3.3). The vertical velocity component Ω is computed at the time level $t = t^{n+1}$ by an appropriate quadrature applied to equation (6) using Du and Dv computed in Step 1 and η computed in Step 2;

Step 4 (§3.4). The values of Ω' at the time level $t = t^{n+1}$ are then obtained from the relaxation step using the (infinitely) fast relaxation.

We note that in *Steps 1–4*, we have used the first-order operator splitting method. One can improve the order of temporal accuracy to the second one by implementing the Strang splitting; see, e.g., [38,39,52].

3.1. Central-upwind scheme for the propagation system (14)

In this section, we develop a semi-discrete second-order central-upwind scheme on prismatic grid for the system (14). In fact, as we mentioned in the beginning of §3, we will only use the developed central-upwind scheme to evolve the discharge components Du and Dv and the auxiliary variable Ω' only.
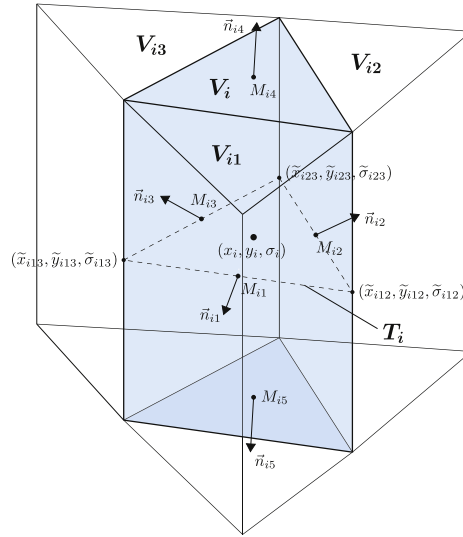
Fig. 1. A typical prismatic cell with three neighbors.

Our choice of the prismatic grid is motivated by the fact that when working in the σ coordinates, the horizontal domain may be arbitrary, while in the vertical direction the domain is always $[-1, 0]$. We therefore use the 2-D triangulation coupled with the uniform grid in the σ-direction with the small scale $\Delta\sigma$. In Fig. 1, we show a typical prismatic cell.

Consider a prismatic cell V_i of volume $|V_i|$ with the centroid (x_i, y_i, σ_i). It has five faces of areas A_{ik}, $k = 1, \ldots, 5$. We denote their corresponding outer unit normals by $\boldsymbol{n}_{ik} := (\cos(\theta_{ik}), \sin(\theta_{ik}), 0)^T$, $k = 1, 2, 3$, $\boldsymbol{n}_{i4} := (0, 0, 1)^T$ and $\boldsymbol{n}_{i5} := (0, 0, -1)^T$; see Fig. 1. We also denote by $M_{ik} = (x_{ik}, y_{ik}, \sigma_{ik})$ the centroid of the k-th face of the cell V_i and by V_{ik} the corresponding neighboring cell, $k = 1, \ldots, 5$.

A semi-discrete scheme for (14) is a system of ODEs for the approximations of the cell averages of the solution:

$$\overline{\boldsymbol{U}}_i(t) \approx \frac{1}{|V_i|} \iiint\limits_{V_i} \boldsymbol{U}(x, y, \sigma, t) \, dx dy d\sigma.$$

For the prismatic cells, a direct extension of the triangular [10,28] and Cartesian [25–27,29,31] second-order central-upwind schemes reads:

$$\begin{aligned}
\frac{d\overline{\boldsymbol{U}}_i}{dt} = &-\frac{1}{|V_i|} \sum_{k=1}^{3} \frac{A_{ik} \cos(\theta_{ik})}{a_{ik}^{\text{in}} + a_{ik}^{\text{out}}} \left[a_{ik}^{\text{in}} \boldsymbol{F}(\boldsymbol{U}_{ik}(M_{ik})) + a_{ik}^{\text{out}} \boldsymbol{F}(\boldsymbol{U}_i(M_{ik})) \right] \\
&- \frac{1}{|V_i|} \sum_{k=1}^{3} \frac{A_{ik} \sin(\theta_{ik})}{a_{ik}^{\text{in}} + a_{ik}^{\text{out}}} \left[a_{ik}^{\text{in}} \boldsymbol{G}(\boldsymbol{U}_{ik}(M_{ik})) + a_{ik}^{\text{out}} \boldsymbol{G}(\boldsymbol{U}_i(M_{ik})) \right] \\
&+ \frac{1}{|V_i|} \sum_{k=1}^{3} A_{ik} \frac{a_{ik}^{\text{in}} a_{ik}^{\text{out}}}{a_{ik}^{\text{in}} + a_{ik}^{\text{out}}} \left[\boldsymbol{U}_{ik}(M_{ik}) - \boldsymbol{U}_i(M_{ik}) \right] \\
&- \frac{1}{\Delta\sigma} \sum_{k=4}^{5} \frac{(-1)^k}{b_{ik}^{\text{in}} + b_{ik}^{\text{out}}} \left[b_{ik}^{\text{in}} \boldsymbol{J}(\boldsymbol{U}_{ik}(M_{ik})) + b_{ik}^{\text{out}} \boldsymbol{J}(\boldsymbol{U}_i(M_{ik})) \right] \\
&+ \frac{1}{\Delta\sigma} \sum_{k=4}^{5} \frac{b_{ik}^{\text{in}} b_{ik}^{\text{out}}}{b_{ik}^{\text{in}} + b_{ik}^{\text{out}}} \left[\boldsymbol{U}_{ik}(M_{ik}) - \boldsymbol{U}_i(M_{ik}) \right] + \overline{\boldsymbol{S}}_i.
\end{aligned} \tag{15}$$

Here, $\boldsymbol{U}_i(M_{ik})$ and $\boldsymbol{U}_{ik}(M_{ik})$ are the reconstructed point values at M_{ik}, $k = 1, 2, 3, 4, 5$, calculated by

$$\boldsymbol{U}_i(M_{ik}) := \lim_{\substack{(x,y,\sigma) \to M_{ik} \\ (x,y,\sigma) \in V_i}} \widetilde{\boldsymbol{U}}(x, y, \sigma), \quad \boldsymbol{U}_{ik}(M_{ik}) := \lim_{\substack{(x,y,\sigma) \to M_{ik} \\ (x,y,\sigma) \in V_{ik}}} \widetilde{\boldsymbol{U}}(x, y, \sigma), \tag{16}$$

where $\widetilde{\boldsymbol{U}}(x, y, \sigma)$ is a piecewise linear reconstruction of $\boldsymbol{U}$ at time t,

$$\widetilde{\boldsymbol{U}}(x, y, \sigma) := \overline{\boldsymbol{U}}_i + (\widehat{\boldsymbol{U}}_x)_i(x - x_i) + (\widehat{\boldsymbol{U}}_y)_i(y - y_i) + (\widehat{\boldsymbol{U}}_\sigma)_i(\sigma - \sigma_i), \quad (x, y, \sigma) \in V_i, \tag{17}$$

in which $(\widehat{\boldsymbol{U}}_x)_i$ and $(\widehat{\boldsymbol{U}}_y)_i$ are approximations of the horizontal derivatives.

To prevent oscillations, the slopes in (17) are to be computed using a nonlinear limiter. To evaluate the horizontal derivatives, $(\widehat{\boldsymbol{U}}_x)_i$ and $(\widehat{\boldsymbol{U}}_y)_i$, we use the limiter developed in [23] (see also [37]) with the small parameter needed to be used to avoid division by zero set to be 10^{-8}; for details, see [37]. To obtain the vertical derivatives, $(\widehat{\boldsymbol{U}}_\sigma)_i$, we use the minmod limiter; see, e.g., [42,46,53,54]. Both limiters are used in a componentwise manner.

The horizontal directional local speeds of propagation, a_{ik}^{in} and a_{ik}^{out}, are defined by

$$a_{ik}^{in} := -\min\left\{\lambda_1[E_{ik}(\boldsymbol{U}_i(M_{ik}), h(M_{ik}))], \lambda_1[E_{ik}(\boldsymbol{U}_{ik}(M_{ik}), h(M_{ik}))], 0\right\},$$
$$a_{ik}^{out} := \max\left\{\lambda_4[E_{ik}(\boldsymbol{U}_i(M_{ik}), h(M_{ik}))], \lambda_4[E_{ik}(\boldsymbol{U}_{ik}(M_{ik}), h(M_{ik}))], 0\right\}, \quad k = 1, 2, 3, \tag{18}$$

where $\lambda_1[E_{ik}] \leq \lambda_2[E_{ik}] \leq \lambda_3[E_{ik}] \leq \lambda_4[E_{ik}]$ are the eigenvalues of the matrix

$$E_{ik}(\boldsymbol{U}, h) = \cos(\theta_{ik})A(\boldsymbol{U}, h) + \sin(\theta_{ik})B(\boldsymbol{U}, h), \quad k = 1, 2, 3. \tag{19}$$

Similarly, the vertical directional local speeds of propagation, b_{ik}^{in} and b_{ik}^{out}, are defined by

$$b_{ik}^{in} := -\min\left\{\lambda_1[C(\boldsymbol{U}_i(M_{ik}), h(M_{ik}))], \lambda_1[C(\boldsymbol{U}_{ik}(M_{ik}), h(M_{ik}))], 0\right\},$$
$$b_{ik}^{out} := \max\left\{\lambda_4[C(\boldsymbol{U}_i(M_{ik}), h(M_{ik}))], \lambda_4[C(\boldsymbol{U}_{ik}(M_{ik}), h(M_{ik}))], 0\right\}, \quad k = 4, 5, \tag{20}$$

where $\lambda_1[C] \leq \lambda_2[C] \leq \lambda_3[C] \leq \lambda_4[C]$ are the eigenvalues of the matrix $C(\boldsymbol{U}, h)$.

Finally, the source terms $\overline{\boldsymbol{S}}_i$ in (15) are to be approximated using a certain quadrature:

$$\overline{\boldsymbol{S}}_i(t) \approx \frac{1}{|V_i|} \iiint\limits_{V_i} \boldsymbol{S}\big(\boldsymbol{U}(x, y, \sigma, t), h(x, y)\big) dx\, dy\, d\sigma.$$

We use a well-balanced quadrature described in §3.1.2 below.

Remark 3.1. All of the evolved and reconstructed indexed quantities in (15)–(20) depend on t, but we suppress this dependence for the sake of brevity.

Remark 3.2. In order to avoid division by 0 (or by a number close to 0), in all of the reported experiments, when $a_{ik}^{in} + a_{ik}^{out} < 10^{-6}$, the scheme (15) has been modified as follows. We first set $a_{ik}^{in} = a_{ik}^{out} = \delta > 0$ in (15) and then pass to the limit as $\delta \to 0$ to obtain

$$\frac{d\overline{\boldsymbol{U}}_i}{dt} = -\frac{1}{|V_i|} \sum_{k=1}^{3} \frac{A_{ik}\cos(\theta_{ik})}{2} \left[\boldsymbol{F}(\boldsymbol{U}_{ik}(M_{ik})) + \boldsymbol{F}(\boldsymbol{U}_i(M_{ik}))\right]$$

$$- \frac{1}{|V_i|} \sum_{k=1}^{3} \frac{A_{ik}\sin(\theta_{ik})}{2} \left[\boldsymbol{G}(\boldsymbol{U}_{ik}(M_{ik})) + \boldsymbol{G}(\boldsymbol{U}_i(M_{ik}))\right]$$

$$- \frac{1}{\Delta\sigma} \sum_{k=4}^{5} \frac{(-1)^k}{2} \left[\boldsymbol{J}(\boldsymbol{U}_{ik}(M_{ik})) + \boldsymbol{J}(\boldsymbol{U}_i(M_{ik}))\right] + \overline{\boldsymbol{S}}_i.$$

A fully discrete scheme can be developed from (15) using a stable ODE solver. In the present study, a three-stage third-order strong stability preserving (SSP) Runge–Kutta solver [18,19,49] was used. The time-step Δt^n is limited by the CFL condition

$$\Delta t^n < \min_{i,k}\left[\min\left\{\frac{r_{ik}}{3\max\left(a_{ik}^{in}, a_{ik}^{out}\right)}, \frac{\Delta\sigma}{2\max\left(b_{ik}^{in}, b_{ik}^{out}\right)}\right\}\right], \tag{21}$$

in which r_{ik}, $k = 1, 2, 3$ are the three corresponding altitudes of the triangular sides of the prismatic cell V_i.

3.1.1. Piecewise linear approximation of the bottom

In this section, we conduct a piecewise linear approximation which is necessary for developing the well-balanced and positivity preserving schemes in the present study. The approach is applicable for both continuous and discontinuous topography function.

We denote by $h_{i\kappa}$ the values of the bottom topography function $H(\widetilde{x}_{i\kappa}, \widetilde{y}_{i\kappa})$ at the vertices $(\widetilde{x}_{i\kappa}, \widetilde{y}_{i\kappa}, \widetilde{\sigma}_{i\kappa})$, $\kappa = 12, 23, 31$, of the horizontal cross-sections of the cell V_i; see Fig. 1.

First, we compute $h_{i\kappa}$ according to the following formula:

$$h_{i\kappa} := \frac{1}{2}\left[\min_{\varrho^2+\zeta^2=1} \lim_{\delta_x,\delta_y\to 0} H\left(\widetilde{x}_{i\kappa} + \delta_x\varrho, \widetilde{y}_{i\kappa} + \delta_y\zeta\right) + \max_{\varrho^2+\zeta^2=1} \lim_{\delta_x,\delta_y\to 0} H\left(\widetilde{x}_{i\kappa} + \delta_x\varrho, \widetilde{y}_{i\kappa} + \delta_y\zeta\right)\right],$$

which is simplified to

$$h_{i\kappa} := H\left(\widetilde{x}_{i\kappa}, \widetilde{y}_{i\kappa}\right)$$

if the function H is continuous at $(\widetilde{x}_{i\kappa}, \widetilde{y}_{i\kappa})$.

The continuous piecewise linear approximation $\widetilde{H}(x, y)$ is then given by

$$\begin{vmatrix} x - \widetilde{x}_{i12} & y - \widetilde{y}_{i12} & \widetilde{H}(x, y) - h_{i12} \\ \widetilde{x}_{i23} - \widetilde{x}_{i12} & \widetilde{y}_{i23} - \widetilde{y}_{i12} & h_{i23} - h_{i12} \\ \widetilde{x}_{i31} - \widetilde{x}_{i12} & \widetilde{y}_{i31} - \widetilde{y}_{i12} & h_{i31} - h_{i12} \end{vmatrix} = 0, \quad (x, y, \sigma) \in V_i. \tag{22}$$

We denote the value of the reconstruction $\widetilde{H}$ at the point M_{ik} by $h_{ik} := \widetilde{H}(M_{ik})$, and at the center of mass (x_i, y_i, σ_i) of V_i by $h_i := \widetilde{H}(x_i, y_i)$, which, as one can easily show, is equal to

$$h_i = \frac{1}{|V_i|} \iiint\limits_{V_i} \widetilde{H}(x, y)\, dxdyd\sigma = \frac{1}{3}(h_{i1} + h_{i2} + h_{i3}) = \frac{1}{3}(h_{i12} + h_{i23} + h_{i31}).$$

3.1.2. Well-balanced discretization of the source term

In order to maintain the "lake at rest" steady states ($\eta \equiv \hat{\eta}$, $u \equiv v \equiv \Omega \equiv 0$, where $\hat{\eta}$ is a constant), an appropriate discretization of the cell average of source term $\overline{S}_i$ has to be developed to exactly balance the numerical fluxes computed by the proposed semi-discrete central-upwind scheme (15). We extend the well-balanced treatment of the 2-D triangular cells in [10] to the studied 3-D model.

Note that at the "lake at rest" steady states, $\boldsymbol{U}_{ik}(M_{ik}) \equiv \boldsymbol{U}_i(M_{ik}) \equiv (\hat{\eta}, 0, 0, 0)^T, \forall i, k$. After a substitution of this "lake at rest" steady state into the right-hand side (RHS) of (15) and taking into account the fact that $a_{ik}^{\mathrm{in}} = a_{ik}^{\mathrm{out}}$, we conclude that the "lake at rest" state will be preserved at the discrete level provided the source quadrature satisfies the following two conditions:

$$-\frac{g}{|V_i|} \sum_{k=1}^{3} A_{ik} \cos(\theta_{ik}) \frac{(\hat{\eta} - h_{ik})^2}{2} + \overline{S}_i^{(2)} = 0, \tag{23}$$

and

$$-\frac{g}{|V_i|} \sum_{k=1}^{3} A_{ik} \sin(\theta_{ik}) \frac{(\hat{\eta} - h_{ik})^2}{2} + \overline{S}_i^{(3)} = 0, \tag{24}$$

where $\overline{\boldsymbol{S}}_i = \left(0, \overline{S}_i^{(2)}, \overline{S}_i^{(3)}, 0\right)^T$ with

$$\overline{S}_i^{(2)} \approx -\frac{g}{|V_i|} \iiint\limits_{V_i} \left(\hat{\eta} - h(x, y)\right) h_x(x, y)\, dxdyd\sigma,$$

$$\overline{S}_i^{(3)} \approx -\frac{g}{|V_i|} \iiint\limits_{V_i} \left(\hat{\eta} - h(x, y)\right) h_y(x, y)\, dxdyd\sigma.$$

In order to derive the desired quadratures, we first apply the divergence theorem

$$\iiint\limits_{V_i} \operatorname{div} \mathcal{G}\, dV = \iint\limits_{\partial V_i} \mathcal{G} \cdot \boldsymbol{n}\, dS,$$

to the vector field $\mathcal{G} = \left(\frac{1}{2}(\eta(x, y) - h(x, y))^2, 0, 0\right)$ and obtain

$$-\iiint\limits_{V_i} (\eta(x, y) - h(x, y)) h_x(x, y)\, dxdyd\sigma = \sum_{k=1}^{3} \iint\limits_{(\partial V_i)_k} \frac{(\eta(x, y) - h(x, y))^2}{2} \cos(\theta_{ik})\, dS$$

$$- \iiint\limits_{V_i} (\eta(x, y) - h(x, y)) \eta_x(x, y)\, dxdyd\sigma. \tag{25}$$

Next, we apply the midpoint rule to the integrals on the RHS of (25) and arrive at the following quadrature for the cell average $\overline{S}_i^{(2)}$:

$$\overline{S}_i^{(2)} = \frac{g}{2|V_i|} \sum_{k=1}^{3} A_{ik} \cos(\theta_{ik}) \left[\frac{\eta_i(M_{ik}) + \eta_{ik}(M_{ik})}{2} - h_{ik} \right]^2 - g(\eta_x)_i(\overline{\eta}_i - h_i), \tag{26}$$

where $(\eta_x)_i$ is the x-slope of the ith piece of the piecewise linear reconstruction of η. Similarly, we obtain the quadrature for the cell average $\overline{S}_i^{(3)}$:

$$\overline{S}_i^{(3)} = \frac{g}{2|V_i|} \sum_{k=1}^{3} A_{ik} \sin(\theta_{ik}) \left[\frac{\eta_i(M_{ik}) + \eta_{ik}(M_{ik})}{2} - h_{ik} \right]^2 - g(\eta_y)_i(\overline{\eta}_i - h_i), \tag{27}$$

where $(\eta_y)_i$ is the y-slope of the ith piece of the piecewise linear reconstruction of η.

Notice that since at "lake at rest" states $(\eta_x)_i \equiv (\eta_y)_i \equiv 0$, $\forall i$ and $\eta_i(M_{ik}) \equiv \hat{\eta}$, $\forall i, k$, the quadratures (26) and (27) satisfy (23) and (24), respectively, as long as $\boldsymbol{U}_i \equiv (\hat{\eta}, 0, 0, 0)^T$.

3.1.3. Nonnegative piecewise linear reconstruction for η

We note that the use of the limited piecewise linear reconstruction (17) for η and piecewise linear approximation (22) of the bottom topography cannot guarantee that the reconstructed values (16) of the water surface level $\eta_i(M_{ik})$ and $\eta_{ik}(M_{ik})$ are above the bed level h_{ik}. This may introduce unphysical negative water depths at M_{ik} and therefore, the piecewise linear reconstruction (17) for η in the problematic cells have to be corrected to ensure the positivity preserving property, that is, that $D_i(M_{ik}) := \eta_i(M_{ik}) - h_{ik} \geq 0$ and $D_{ik}(M_{ik}) := \eta_{ik}(M_{ik}) - h_{ik} \geq 0$.

In this section, we extend the 2-D correction algorithm from [10] to the studied 3-D SWEs. By modifying $\widetilde{\eta}$, we will in fact guarantee that $\widetilde{\eta}(x, y) \geq \widetilde{H}(x, y)$ throughout the entire computational domain.

The correction is performed as follows. First, for the dry cells in which $\overline{\eta}_i = h_i$, we simply set $\widetilde{\eta}(x, y) = \widetilde{H}(x, y)$. For the wet cells in which $\overline{\eta}_i > h_i$, the following two problematic cases are possible.

• Case 1: There is only one vertex, say, with index $\kappa = 12$, for which $\eta_i(\widetilde{x}_{i\kappa}, \widetilde{y}_{i\kappa}) < h_{i\kappa}$. In this case, we first correct this physically irrelevant reconstructed value by setting $\eta_i(\widetilde{x}_{i12}, \widetilde{y}_{i12}) = h_{i12}$. Next, we determine $\eta_i(\widetilde{x}_{i\kappa}, \widetilde{y}_{i\kappa})$ at the remaining two vertices with $\kappa = 23$ and 31 by setting $\eta_i(\widetilde{x}_{i23}, \widetilde{y}_{i23}) - h_{i23} = \eta_i(\widetilde{x}_{i31}, \widetilde{y}_{i31}) - h_{i31}$. Then, the conservation requirement yields

$$\eta_i(x_{i23}, y_{i23}) - h_{i23} = \eta_i(x_{i31}, y_{i31}) - h_{i31} = \frac{3}{2}(\overline{\eta}_i - h_i), \tag{28}$$

and the original reconstruction (17) for η is replaced with a new one defined by

$$\begin{vmatrix} x - x_i & y - y_i & \widetilde{\eta}(x, y) - \overline{\eta}_i \\ \widetilde{x}_{i12} - x_i & \widetilde{y}_{i12} - y_i & h_{i12} - \overline{\eta}_i \\ \widetilde{x}_{i23} - x_i & \widetilde{y}_{i23} - y_i & \frac{3}{2}(\overline{\eta}_i - h_i) + h_{i23} - \overline{\eta}_i \end{vmatrix} = 0, \quad (x, y) \in V_i. \tag{29}$$

• Case 2: There are two vertices, say, with indices $\kappa = 12$ and 23, for which $\eta_i(\widetilde{x}_{i\kappa}, \widetilde{y}_{i\kappa}) < h_{i\kappa}$. In this case, we first correct these two physically irrelevant reconstructed values by setting $\eta_i(\widetilde{x}_{i12}, \widetilde{y}_{i12}) = h_{i12}$ and $\eta_i(\widetilde{x}_{i23}, \widetilde{y}_{i23}) = h_{i23}$. Then, the conservation requirement yields

$$\eta_i(\widetilde{x}_{i31}, \widetilde{y}_{i31}) - h_{i31} = 3(\overline{\eta}_i - h_i), \tag{30}$$

and the original reconstruction (17) for η is replaced with a new one defined by

$$\begin{vmatrix} x - x_i & y - y_i & \widetilde{\eta}(x, y) - \overline{\eta}_i \\ \widetilde{x}_{i12} - x_i & \widetilde{y}_{i12} - y_i & h_{i12} - \overline{\eta}_i \\ \widetilde{x}_{i31} - x_i & \widetilde{y}_{i31} - y_i & 3(\overline{\eta}_i - h_i) + h_{i31} - \overline{\eta}_i \end{vmatrix} = 0, \quad (x, y) \in V_i. \tag{31}$$

Equipped with the positivity preserving reconstruction $\widetilde{\eta}$, the point values of the velocities u and v needed in the computation of the one-sided local speeds in (18) and (20) are recalculated using the same desingularization procedure as in [10,29]; namely (the i, k indexes are omitted):

$$u = \frac{\sqrt{2} \, D \, (Du)}{\sqrt{D^4 + \max(D^4, \varphi)}}, \quad v = \frac{\sqrt{2} \, D \, (Dv)}{\sqrt{D^4 + \max(D^4, \varphi)}},$$

where φ is a prescribed tolerance (in all of the numerical experiments reported below we have used $\varphi = 10^{-10}$). After obtaining the desingularized point values of u and v, we recompute the x- and y-discharges and fluxes accordingly, that is, we set

$$(Du) := D \cdot u, \qquad (Dv) := D \cdot v,$$

$$\boldsymbol{F} = \left((Du), (Du) \cdot u + \frac{g}{2} D^2, (Du) \cdot v, 0 \right)^T,$$

$$\boldsymbol{G} = \left((Dv), (Dv) \cdot u, (Dv) \cdot v + \frac{g}{2} D^2, 0 \right)^T,$$

$$\boldsymbol{J} = \left(\Omega', u \cdot \Omega', v \cdot \Omega', W^* \Omega' \right)^T,$$

at the points where these quantities are to be calculated.

3.2. Central-upwind scheme for the depth-averaged Equation (5)

We evolve the water surface elevation η by applying the "triangular" central-upwind scheme from [10,28] to the vertically integrated free surface equation (5):

$$\frac{d\overline{\eta}_i}{dt} = -\frac{1}{|T_i|} \sum_{k=1}^{3} \frac{\ell_{ik} \cos(\theta_{ik})}{a_{ik}^{\text{in}} + a_{ik}^{\text{out}}} \left[a_{ik}^{\text{in}} \big((\mathring{D}u)_{ik}(M_{ik}) \big) + a_{ik}^{\text{out}} \big((\mathring{D}u)_i(M_{ik}) \big) \right]$$

$$- \frac{1}{|T_i|} \sum_{k=1}^{3} \frac{\ell_{ik} \sin(\theta_{ik})}{a_{ik}^{\text{in}} + a_{ik}^{\text{out}}} \left[a_{ik}^{\text{in}} \big((\mathring{D}v)_{ik}(M_{ik}) \big) + a_{ik}^{\text{out}} \big((\mathring{D}v)_i(M_{ik}) \big) \right]$$

$$+ \frac{1}{|T_i|} \sum_{k=1}^{3} \ell_{ik} \frac{a_{ik}^{\text{in}} a_{ik}^{\text{out}}}{a_{ik}^{\text{in}} + a_{ik}^{\text{out}}} \left[\eta_{ik}(M_{ik}) - \eta_i(M_{ik}) \right]. \tag{32}$$

Here, T_i is the triangular horizontal cross-section of the prism V_i; ℓ_{ik}, $k = 1, 2, 3$ are the lengths of the corresponding sides of the triangle T_i; $\mathring{D}u$ and $\mathring{D}v$ are vertically integrated fluxes calculated as follows. We first compute the vertically averaged quantities

$$(\overline{\mathring{D}u}) = \sum_{m:\,(x_m, y_m) = (x_i, y_i)} (\overline{Du})_m \, \Delta\sigma, \qquad (\overline{\mathring{D}v}) = \sum_{m:\,(x_m, y_m) = (x_i, y_i)} (\overline{Dv})_m \, \Delta\sigma,$$

which are then used to obtain the required point values $(\mathring{D}u)_i(M_{ik})$ and $(\mathring{D}v)_i(M_{ik})$ for $k = 1, 2, 3$ using piecewise linear reconstruction (17), (16) with $\sigma = \sigma_i$ and the limiter developed in [23]. Finally, the one-sided local speeds a_{ik}^{in} and a_{ik}^{out} are calculated using equations (18) and (19) with Du and Dv replaced with $\mathring{D}u$ and $\mathring{D}v$, respectively.

Remark 3.3. As before, we avoid division by 0 (or by a number close to 0), by replacing the scheme (32) with

$$\frac{d\overline{\eta}_i}{dt} = -\frac{1}{|T_i|} \sum_{k=1}^{3} \frac{\ell_{ik} \cos(\theta_{ik})}{2} \left[\big((\mathring{D}u)_{ik}(M_{ik}) \big) + \big((\mathring{D}u)_i(M_{ik}) \big) \right]$$

$$- \frac{1}{|T_i|} \sum_{k=1}^{3} \frac{\ell_{ik} \sin(\theta_{ik})}{2} \left[\big((\mathring{D}v)_{ik}(M_{ik}) \big) + \big((\mathring{D}v)_i(M_{ik}) \big) \right],$$

whenever $a_{ik}^{\text{in}} + a_{ik}^{\text{out}} < 10^{-6}$.

Remark 3.4. The use of the continuous piecewise linear approximation of the bottom (see §3.1.1) and a nonnegative piecewise linear reconstruction of the water surface (see §3.1.3) guarantees the positivity preserving property of the presented scheme. Following the proof in [10], one can establish the following positivity preserving result.

Theorem 3.1. *Consider equation* (5) *and the semi-discrete central-upwind scheme* (32) *with the nonnegative piecewise linear reconstruction of the water surface presented in §3.1.3. Assume that the system of ODEs* (32) *is solved by either the forward Euler method or an SSP Runge–Kutta solver and that for all i, $\overline{\eta}_i(t^n) - h_i \geq 0$ at time $t = t^n$. Then, for all i, $\overline{\eta}_i(t^{n+1}) - h_i \geq 0$ at time $t = t^{n+1}$, provided that*

$$\Delta t^n \leq \min_{i,k} \left\{ \frac{r_{ik}}{6 \max \left(a_{ik}^{\text{in}}, a_{ik}^{\text{out}} \right)} \right\}, \tag{33}$$

where r_{ik}, $k = 1, 2, 3$ are, as in (21)*, the three corresponding altitudes of the triangle T_i.*

Notice that the positivity preserving requirement together with the CFL condition (21) yields the following restriction on the time-step size:

$$\Delta t^n \leq \min_{i,k} \left[\min \left\{ \frac{r_{ik}}{6 \max\left(a_{ik}^{\text{in}}, a_{ik}^{\text{out}}\right)}, \frac{\Delta\sigma}{2 \max\left(b_{ik}^{\text{in}}, b_{ik}^{\text{out}}\right)} \right\} \right], \tag{34}$$

and for all the numerical tests in this study, we use the maximum value of the restriction (34) as Δt^n.

3.3. Numerical scheme for updating the vertical velocity Ω

After the water surface η and discharges Du and Dv have been evolved from time level $t = t^n$ to the new time level $t = t^{n+1}$, we use the obtained values to update the vertical velocity Ω as it is described in this section.

Let us assume that the $[-1, 0]$ interval is split into L uniform subintervals so that $\sigma_m := -1 + \Delta\sigma/L$, $m = 0, \ldots, L$. We consider a prismatic cell V_i with the horizontal surfaces $\sigma = \sigma_m$ (top) and $\sigma = \sigma_{m-1}$ (bottom) for some $m \in \{1, \ldots, L\}$. Then, sampling equation (6) at time $t = t^{n+1}$ and at $\sigma = \sigma_m$ and $\sigma = \sigma_{m-1}$ and subtracting one from the other results in

$$\frac{1}{|T_i|} \int_{T_i} \left[\Omega(x, y, \sigma_m, t^{n+1}) - \Omega(x, y, \sigma_{m-1}, t^{n+1}) \right] dxdy$$
$$= -\frac{1}{|T_i|} \int_{T_i} \left[\eta_t(x, y, t^{n+1}) + \int_{\sigma_{m-1}}^{\sigma_m} \left\{ (Du)_x(x, y, \sigma, t^{n+1}) + (Dv)_y(x, y, \sigma, t^{n+1}) \right\} d\sigma \right] dxdy. \tag{35}$$

Introducing the horizontal cell averages

$$\overline{\Omega}_i^m(t) := \frac{1}{|T_i|} \int_{T_i} \Omega(x, y, \sigma_m, t) \, dxdy,$$

using the second-order backward difference approximation of η_t, the central-upwind approximation of the $(Du)_x$ and $(Dv)_y$ terms, and the midpoint quadrature, equation (35) yields

$$\overline{\Omega}_i^m(t^{n+1}) = \overline{\Omega}_i^{m-1}(t^{n+1}) - \frac{\Delta\sigma}{2\Delta t^n} \left[3\overline{\eta}_i(t^{n+1}) - 4\overline{\eta}_i(t^n) + \overline{\eta}_i(t^{n-1}) \right]$$
$$- \frac{1}{|V_i|} \sum_{k=1}^{3} \frac{A_{ik} \cos(\theta_{ik})}{a_{ik}^{\text{in}} + a_{ik}^{\text{out}}} \left[a_{ik}^{\text{in}}\left((Du)_{ik}(M_{ik})\right) + a_{ik}^{\text{out}}\left((Du)_i(M_{ik})\right) \right]$$
$$- \frac{1}{|V_i|} \sum_{k=1}^{3} \frac{A_{ik} \sin(\theta_{ik})}{a_{ik}^{\text{in}} + a_{ik}^{\text{out}}} \left[a_{ik}^{\text{in}}\left((Dv)_{ik}(M_{ik})\right) + a_{ik}^{\text{out}}\left((Dv)_i(M_{ik})\right) \right]$$
$$+ \frac{1}{|V_i|} \sum_{k=1}^{3} A_{ik} \frac{a_{ik}^{\text{in}} a_{ik}^{\text{out}}}{a_{ik}^{\text{in}} + a_{ik}^{\text{out}}} \left[\eta_{ik}(M_{ik}) - \eta_i(M_{ik}) \right], \tag{36}$$

where all of the quantities in the last three sums on the RHS of (36) are computed according to the algorithm described in §3.1, but using the data at the new time level $t = t^{n+1}$.

We note that the boundary condition $\Omega(x, y, \sigma = 0, t) = 0$ implies that for all cells V_i located at the bottom of the computational domain, $\overline{\Omega}_i^0(t^{n+1}) = 0$, and thus all of the values of $\overline{\Omega}_i^m(t^{n+1})$ can be recursively obtained from (36). Finally, we use the trapezoidal rule in the σ-direction to conclude with

$$\overline{\Omega}_i(t^{n+1}) = \frac{1}{2} \left[\overline{\Omega}_i^m(t^{n+1}) + \overline{\Omega}_i^{m-1}(t^{n+1}) \right], \tag{37}$$

where, as before,

$$\overline{\Omega}_i(t^{n+1}) \approx \frac{1}{|V_i|} \int_{V_i} \Omega(x, y, \sigma, t) \, dxdyd\sigma.$$

Remark 3.5. We note that at the first time-step, the second-order temporal discretization of η_t in (36) should be replaced with the first-order one, $\frac{\Delta\sigma}{\Delta t^n} \left[\overline{\eta}_i(t^{n+1}) - \overline{\eta}_i(t^n) \right]$.

3.4. Fast relaxation step

Recall that upon completion of the evolution step described in §3.1, the intermediate values $(\overline{\Omega_i'})^*$ are obtained and are now to be corrected by numerically solving the relaxation equation

$$\Omega_t' = -\frac{1}{\varepsilon}(\Omega' - \Omega). \tag{38}$$

Since $\varepsilon > 0$ is a very small relaxation parameter, equation (38) is very stiff and we discretize it using the implicit backward Euler method:

$$\overline{\Omega_i'}(t^{n+1}) = (\overline{\Omega_i'})^* - \frac{\Delta t^n}{\varepsilon}\left[\overline{\Omega_i'}(t^{n+1}) - \overline{\Omega_i}(t^{n+1})\right], \tag{39}$$

where $\overline{\Omega_i}(t^{n+1})$ is given by (37). Equation (39) is a linear equation on $\overline{\Omega_i'}(t^{n+1})$ and it can be explicitly solved to obtain

$$\overline{\Omega_i'}(t^{n+1}) = \frac{\varepsilon(\overline{\Omega_i'})^* + \Delta t^n \overline{\Omega_i}(t^{n+1})}{\varepsilon + \Delta t^n}. \tag{40}$$

Notice that, taking the limit as $\varepsilon \to 0+$ in (40) leads to the infinitely fast relaxation, which results in

$$\overline{\Omega_i'}(t^{n+1}) = \overline{\Omega_i}(t^{n+1}),$$

that is, $\Omega' = \Omega$ throughout the entire computational domain. Our numerical experiments clearly indicate that the proposed method is insensitive to the choice of small parameter ε and therefore in all of the numerical results reported in §4, we have used the infinitely fast relaxation.

4. Numerical experiments

In this section, we demonstrate the performance of the proposed well-balanced and positivity preserving central-upwind scheme on five numerical examples.

In Examples 3–5, we modify the discharge equations (8) and (9) by including the vertical diffusion terms so that the modified discharge equations read as

$$\begin{aligned}
(Du)_t + \left(Du^2 + \frac{g}{2}D^2\right)_x + (Duv)_y + (\Omega'u)_\sigma &= -gDh_x + \left(\frac{\nu_v}{D}u_\sigma\right)_\sigma, \\
(Dv)_t + (Duv)_x + \left(Dv^2 + \frac{g}{2}D^2\right)_y + (\Omega'v)_\sigma &= -gDh_y + \left(\frac{\nu_v}{D}v_\sigma\right)_\sigma,
\end{aligned} \tag{41}$$

where ν_v is the vertical eddy viscosity.

We approximate the vertical diffusion terms in the flux form using centered differences. At the top of the computational domain, the centered-difference approximations are replaced with the one-sided ones, while at the bottom, we replace the vertical gradients u_σ and v_σ with τ_x/ρ and τ_y/ρ, where ρ is the water density and τ_x and τ_y represent the bottom stress, which is determined using a quadratic law as follows:

$$\tau_x = \rho\, C_f u_b \left(u_b^2 + v_b^2\right)^{\frac{1}{2}}, \quad \tau_y = \rho\, C_f v_b \left(u_b^2 + v_b^2\right)^{\frac{1}{2}}.$$

Here, u_b and v_b are velocities at the bottom and C_f is an empirical coefficient of the bottom friction.

In the numerical examples below, we take the following parameter values:

$$g = 9.81\ \text{m/s}^2, \quad \rho = 1000\ \text{kg/m}^3,$$

and estimate the vertical eddy viscosity by a two-layer mixing length model [45]:

$$\nu_v = \left(\frac{\ell_m}{D}\right)^2 \left(u_\sigma^2 + v_\sigma^2\right)^{\frac{1}{2}},$$

where the mixing length ℓ_m can be estimated by

$$\ell_m = \begin{cases} 0.4(\sigma + 1)D, & \text{if } \sigma \leq -0.75, \\ 0.1D, & \text{otherwise.} \end{cases}$$
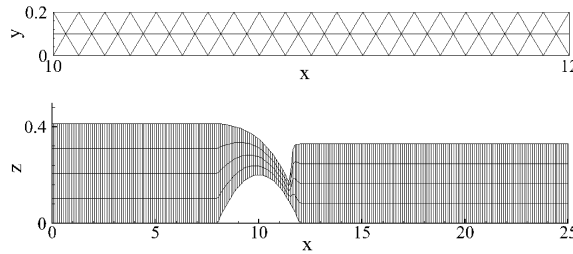
Fig. 2. Example 1: The horizontal (top) and vertical (bottom) mesh at the steady state.

4.1. Example 1—transcritical flow over a hump

In this numerical example taken from [20,55], we test the ability of the proposed numerical method to accurately capture hydraulic jump.

We numerically solve the 3-D SWEs with $g = 9.81$ and the bottom topography defined by

$$h(x, y) = \begin{cases} 0.2 - 0.05(x - 10)^2, & \text{if } 8 \leq x \leq 12, \\ 0, & \text{otherwise}, \end{cases}$$

on the computational domain $[0, 25] \times [0, 0.2] \times [-1, 0]$ discretized using prismatic cells of average volume 0.00125 with 4 vertical layers (Fig. 2 shows the horizontal and vertical arrangement of the mesh).

We study the convergence of the computed solution in time towards steady flow. The solution is considered to be convergent if the following condition [57] is satisfied:

$$\sum_i \left(\frac{\overline{D}_i^n - \overline{D}_i^{n-1}}{\overline{D}_i^n} \right)^2 < 10^{-12}.$$

We consider the following set of initial and boundary data:

$$\eta(x, y, 0) = 0.33, \quad (Du)(x, y, \sigma, 0) = 0, \quad (Dv)(x, y, \sigma, 0) = 0, \quad \Omega(x, y, \sigma, 0) = 0,$$
$$(Du)(0, y, \sigma, t) = q_0 = 0.18, \quad (Dv)(0, y, \sigma, t) = 0, \quad \eta(25, y, t) = \eta_{25} = 0.33,$$

which corresponds to the transcritical steady flow with a shock.

The steady state analytical solutions, given in [20,15], can be obtained as follows. The discharges are $(Du) \equiv q_0$ and $(Dv) \equiv 0$, the water depth D is obtained by solving the Bernoulli equations

$$\begin{cases} D^3 + [h(x, y) - \dfrac{q_0^2}{2gD_c^2} - D_c - h_M]D^2 + \dfrac{q_0^2}{2g} = 0, & \text{if } x < x_{sh}, \\ D^3 + [h(x, y) - \dfrac{q_0^2}{2gD_b^2} - D_b]D^2 + \dfrac{q_0^2}{2g} = 0, & \text{if } x > x_{sh}, \end{cases} \qquad (42)$$

where $D_c = \left[q_0 / \sqrt{g} \right]^{2/3}$, $h_M = \max_{x \in [0,25]} h(x, y)$, $D_b = \eta_{25} - h(25, y)$, and x_{sh} is the location of the shock that can be determined using the Rankine–Hugoniot condition

$$q_0^2 \left(\frac{1}{D_L} - \frac{1}{D_R} \right) + \frac{g}{2}(D_L^2 - D_R^2) = 0,$$

where $D_L := D(x \to x_{sh}^-, y)$ and $D_R := D(x \to x_{sh}^+, y)$ at the steady state.

Fig. 3 (top) demonstrates a very good agreement between the computed and analytical values of the water surface. Fig. 3 (bottom) shows that when the computed and analytical values of the discharge are compared, they also agree quite well though some oscillations can be observed near the turning point of water surface. In the steady state, the root-mean-square relative errors for the simulated water level and x-discharge are 2.61% and 2.98%, respectively, which reduce to 0.86% and 0.91%, respectively, when the prismatic cells of average volume 0.000625 with 4 vertical layers are used.

4.2. Example 2—wind-induced water circulation

In this example, we test the accuracy of the proposed numerical method in predicting the vertical distribution of velocity. We simulate the wind-induced water circulation in an rectangular closed basin.
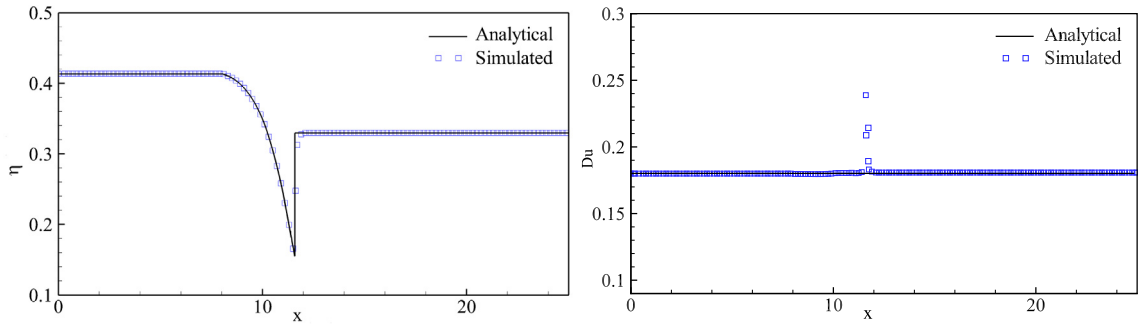
Fig. 3. Example 1: Comparison between the computed and analytical steady states for the water surface level η (left) and discharge Du (right).
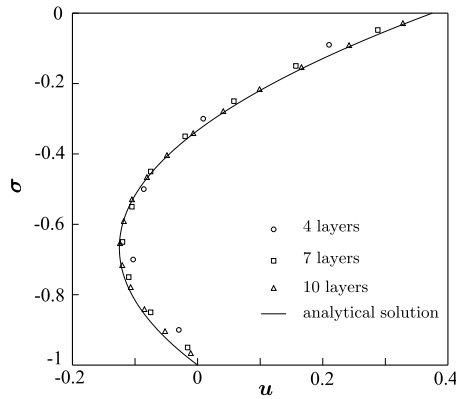

Fig. 4. Example 2: The numerical solution $u(\sigma, 200)$ computed using different number of vertical layers and the analytical (solid line) steady-state solution.

In this numerical experiment, we simplify the 3-D SWEs by neglecting the horizontal advection terms and setting both the bottom topography and water surface to be flat so that $h = $ Const and $D = $ Const. At the same time, we include the vertical diffusion terms as in (41), so that the studied relaxation system becomes

$$(Du)_t + (\Omega' u)_\sigma = \left(\frac{\nu_v}{D} u_\sigma\right)_\sigma,$$

$$(Dv)_t + (\Omega' v)_\sigma = \left(\frac{\nu_v}{D} v_\sigma\right)_\sigma,$$

$$\Omega'_t + W^* \Omega'_\sigma = -\frac{1}{\varepsilon}(\Omega' - \Omega).$$

We take the following parameter values:

$$\frac{\nu_v}{D} = 0.001, \quad \tau_x \equiv 1.5, \quad \tau_y \equiv 0,$$

for which the analytical steady-state solution is (see [21]):

$$u(\sigma) = \frac{D\tau_x(\sigma + 1)(3\sigma + 1)}{4\rho\nu_v}, \quad v(\sigma) \equiv 0.$$

We run the simulations using the zero initial conditions ($u(\sigma, 0) \equiv v(\sigma, 0) \equiv \Omega(\sigma, 0) \equiv 0$) and compute the solution until the final time $t = 200$, by which the solution is very close to its steady state. The simulation results obtained using evenly distributed 4, 7 and 10 layers are compared with the analytical solution in Fig. 4. As one can see, the computed solutions are in good agreement with the analytical one and the accuracy is improved with higher resolution in the vertical direction. The root-mean-square relative errors for the simulations with 4, 7 and 10 layers are 7.7%, 2.5% and 1.3%, respectively.

4.3. Example 3—small perturbation of a "lake at rest" steady state

In this example, we demonstrate importance of the well-balanced property of the developed numerical method.

We consider the 3-D version of the initial value problem (IVP), which is a modification of the benchmark originally proposed in [32]. We solve the 3-D SWEs on the computational domain is $[0, 20] \times [0, 10] \times [-1, 0]$. The bottom topography is an elliptical shaped hump defined by
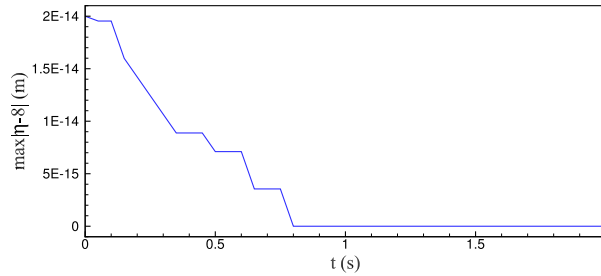
Fig. 5. Example 3, $\phi = 2 \cdot 10^{-14}$: $\max\limits_{x,y} |\eta - 8|$ computed on a coarse grid as a function of t.

$$h(x, y) = 7.8 \exp\left[-0.05(x - 10)^2 - 0.2(y - 5)^2\right].$$

The initial conditions are

$$\eta(x, y, 0) = \begin{cases} 8 + \phi, & \text{if } 0.05 < x < 0.15, \\ 8, & \text{otherwise,} \end{cases} \quad u(x, y, \sigma, 0) \equiv v(x, y, \sigma, 0) \equiv \Omega(x, y, \sigma, 0) \equiv 0,$$

where ϕ is the height of a small perturbation of the water surface. Zero-order extrapolation is used at the right and left boundaries, while periodic boundary conditions are set in the y-direction. The bottom friction coefficient is set to $C_f = 0.02$.

We first take a very small $\phi = 2 \cdot 10^{-14}$, which is comparable with the machine error, and numerically verify the well-balanced property of the proposed numerical method. In Fig. 5, we plot $\max\limits_{x,y} |\eta - 8|$ as a function of t, computed on a coarse mesh using 800 triangles in the horizontal cross section and 5 vertical layers. As one can clearly see, no instabilities are developed and the balance between the fluxes and source terms is numerically preserved.

We then take a larger, but still very small perturbation height $\phi = 0.004$. Fig. 6 displays the right-going disturbance as it propagates past the hump. The water surface, $\eta(x, y, t)$, computed on the mesh using 20000×8 prismatic cells, is presented at times $t = 0.3$, 0.6, 0.9, 1.2, 1.5 and 1.9. It can be observed that in the downstream area of the perturbation, the proposed well-balanced numerical method preserve the "lake at rest" structure.

Fig. 7 shows the water surfaces computed by the well-balanced and non-well-balanced methods, respectively, at $t = 0.3$ and 1.9 on the same 20000×8 grid. The non-well-balanced method, obtained by replacing the well-balanced quadratures (26) and (27) by straightforward midpoint rule discretizations:

$$\overline{S}_i^{(2)} = -g(\overline{\eta}_i - h_i)(h_x)_i, \qquad \overline{S}_i^{(3)} = -g(\overline{\eta}_i - h_i)(h_y)_i,$$

where $(h_x)_i$ and $(h_y)_i$ are the slopes of the piecewise linear approximation of the bottom topography given by (22). As one can clearly see, the well-balanced method can preserve the quiescent water status in the downstream area, while the solution, computed by the non-well-balanced scheme generates spurious waves over the irregular bed, which are of about the same or even larger magnitude than the waves generated by the small perturbation.

4.4. Example 4—dam break wave propagating over an island

This test is designed to verify the positivity preserving properties and the ability to simulate sharp gradient of the proposed numerical method by simulating a shallow overtopping wave developed from a dam-break flow.

We solve the 3-D SWEs on the computational domain is $[0, 4] \times [0, 2] \times [-1, 0]$. The bottom topography is defined by

$$h(x, y) = 0.4 \exp\left[-1(x - 2)^2 - 2(y - 1)^2\right].$$

The initial conditions are

$$\eta(x, y, 0) = \begin{cases} 0.5, & \text{if } x < 0.3, \\ 0.3, & \text{otherwise,} \end{cases} \quad u(x, y, \sigma, 0) \equiv v(x, y, \sigma, 0) \equiv \Omega(x, y, \sigma, 0) \equiv 0,$$

so that the wave will travel in the positive x-direction past an elliptical shaped island. During this process, a very shallow overtopping flow will occur at the time when a small portion of the wave washes over the island and introduces a very small water depth on the initial dry island. The wetting and drying process is also involved during the simulation. The bottom friction coefficient is set to $C_f = 0.01$.

Fig. 8 shows the surface waves computed by the proposed numerical method at different times using 20000×5 prismatic cells. As one can see, no spurious waves are generated and no instabilities are developed when a very shallow wave washes over the initially dry island. In Fig. 9, a detailed plot of the computed velocity field at different times is shown when the wave travels past the island. As one can see, the proposed method is stable and captures the wash over region without any unphysical oscillations.
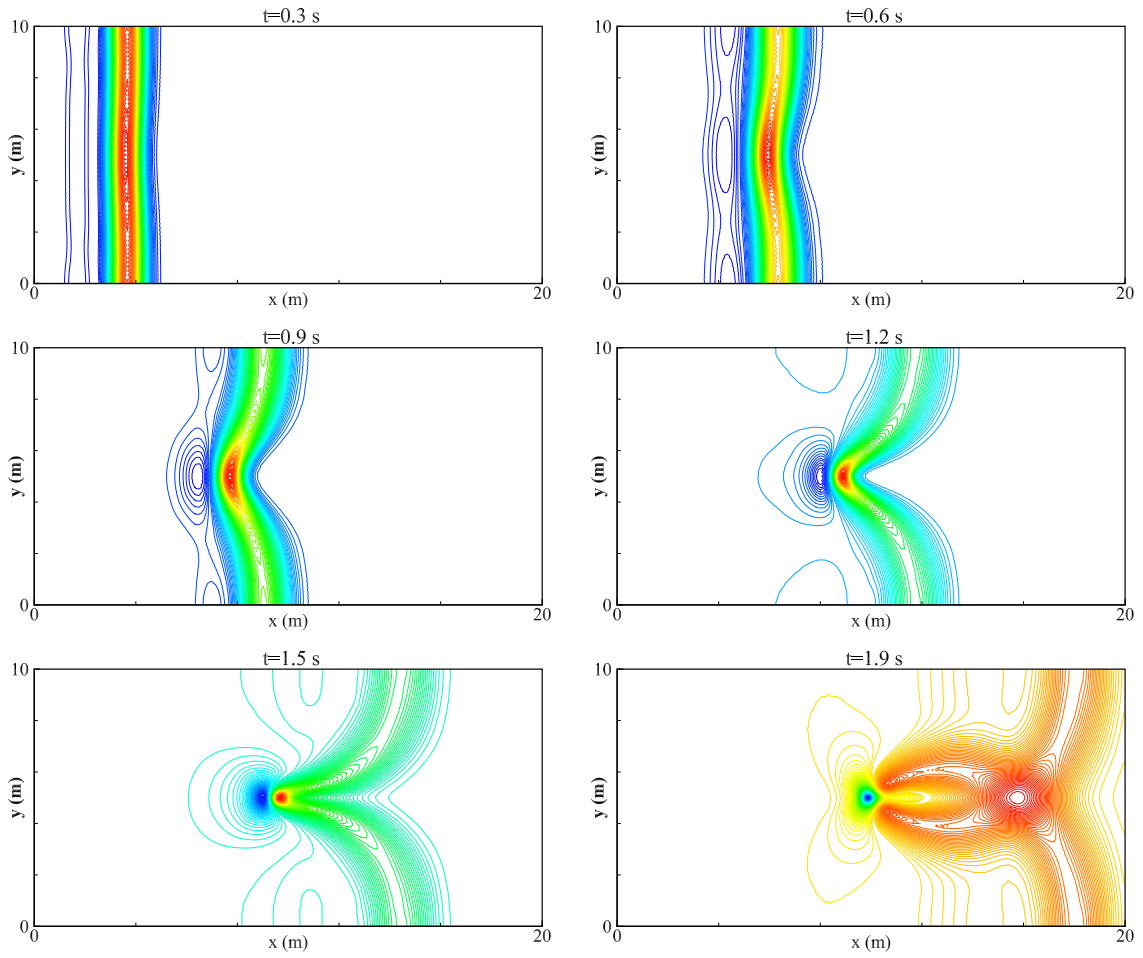
Fig. 6. Example 3, $\phi = 4 \cdot 10^{-3}$: The η component of the solution computed by the proposed well-balanced numerical method.
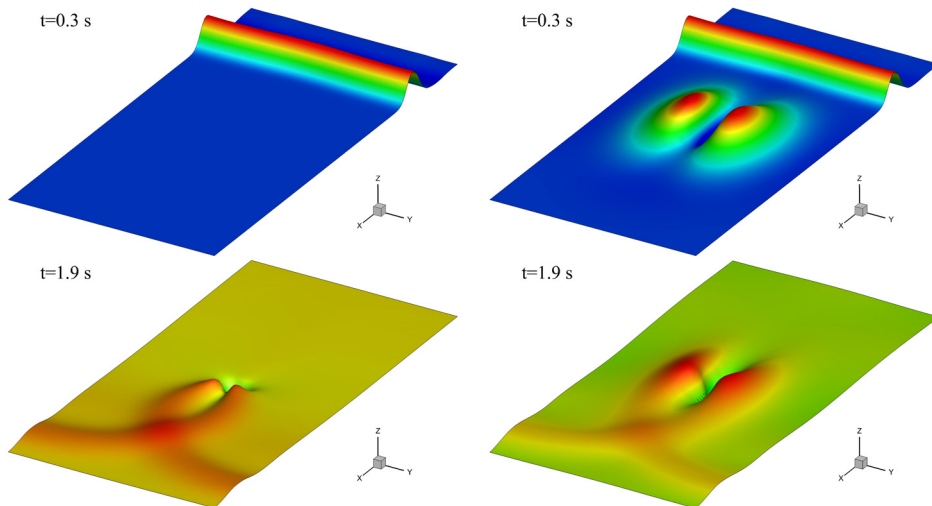
Fig. 7. Example 3, $\phi = 4 \cdot 10^{-3}$: The water surface computed by the well-balanced (left column) and non-well-balanced (right column) methods at $t = 0.3$ and 1.9.
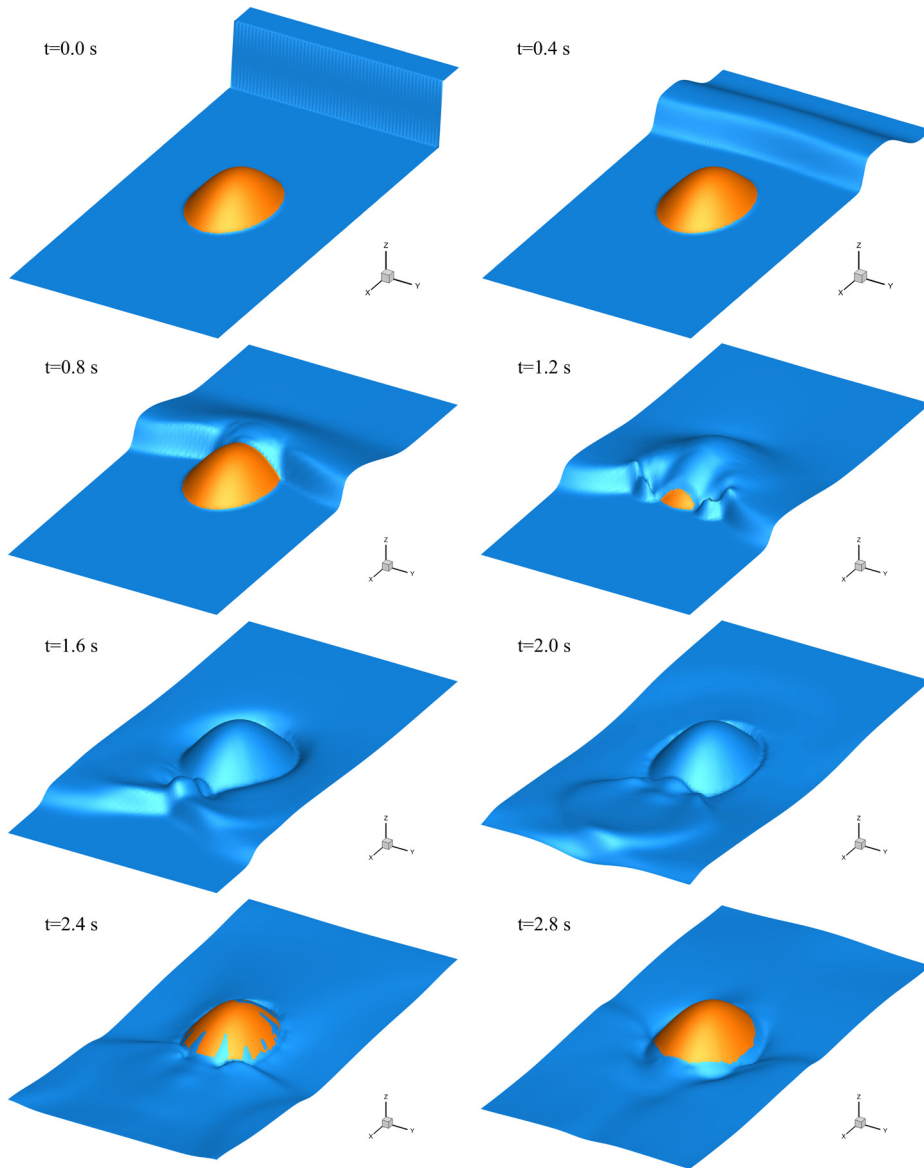
Fig. 8. Example 4: The η component of the solution computed at different times.

4.5. Example 5—laboratory dam-break flow over a triangular hump

In the last numerical example, the accuracy and positivity preserving property of the proposed numerical method are tested by simulating a laboratory dam-break flow over a triangular hump in a long straight flume. This experiment is originally reported in [41], and has been used in [8,34] to validate numerical models.

The experimental setup described in [41] is schematically shown in Fig. 10. At time $t = 0$, the dam is located at $x = 15.5$ m in a 38 m long flume; the reservoir in the upstream is initially filled with water of 0.75 m deep; an initial dry bed is used in the downstream of the reservoir and a symmetric triangular hump of 0.4 m high is installed between $x = 25.5$ m and $x = 31.5$ m. The upstream end is a solid wall and the downstream end is a free outlet. The flow depth was measured by several gauges including Gauge 1, Gauge 2, Gauge 3, Gauge 4, Gauge 5 and Gauge 6, located at 2 m, 4 m, 8 m, 10 m, 11 m and 13 m, respectively, downstream from the dam.

We compute the solution until the final time $t = 90$ on the computational domain $[0, 38] \times [0, 0.2] \times [-1, 0]$ using 11400×4 prismatic cells. The bottom friction coefficient is set to $C_f = 0.012$. Fig. 11 shows the comparison between the computed and measured water depths over 90 s at the aforementioned 6 gauge points. It can be seen that the simulated results are in quite good agreement with the laboratory data at all of the gauge points in terms of arriving time and water depth. Small discrepancies of maximum water depth are observed between the predicted results and experimental
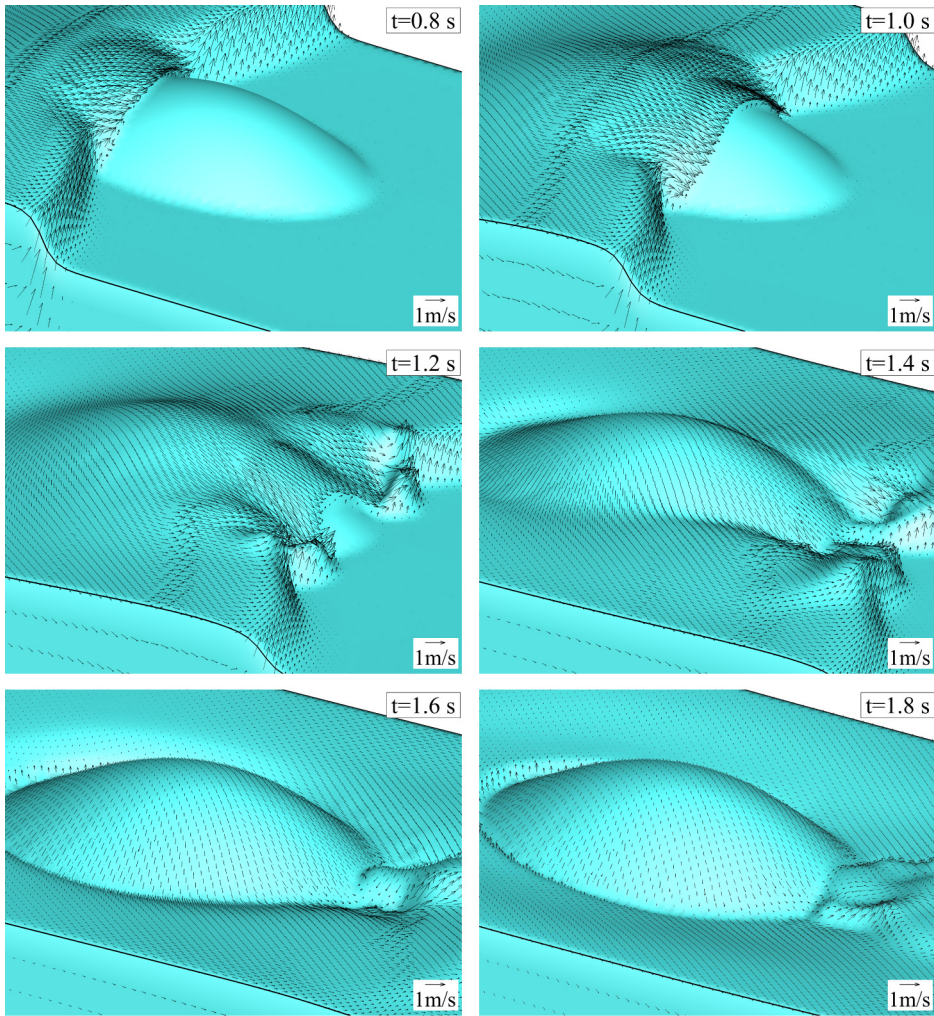
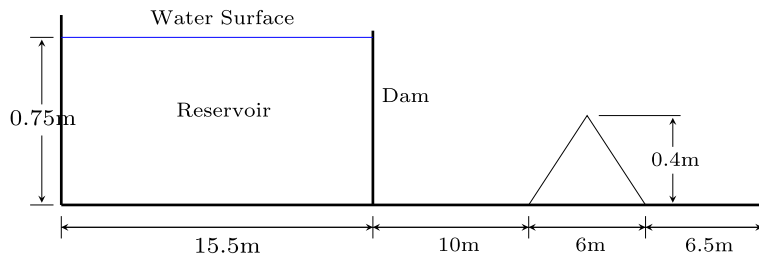**Fig. 9.** Example 4: The computed velocities of the wave washing over the island.

Fig. 10. Example 5: Experimental setup of the laboratory dam-break flow.

measurements at gauges 3 and 4. Such discrepancies have been also observed by other researchers using different numerical schemes in [8,34]. A possible explanation for such disagreements is that the flow at the upstream toe of the triangular hump is highly turbulent and complex at times 16–18 s when the falling wave from upstream slope of the hump meets the right-propagating wave near the junction of the upstream face of the triangular hump with flat bed, and the shallow water equations with hydrostatic assumption may not be accurate enough for describing such situations.

In Fig. 12, we take a closer look at the wave front when it runs up the initially dry triangular hump at $t = 4$. As one can see, no unphysically large or spurious velocity is generated near the front. This confirms that the positivity preserving reconstruction successfully maintains stability in the areas with a small water depth. The effect of the bottom friction is also clearly demonstrated as one can see that the closer to the bottom, the smaller the velocity magnitude.
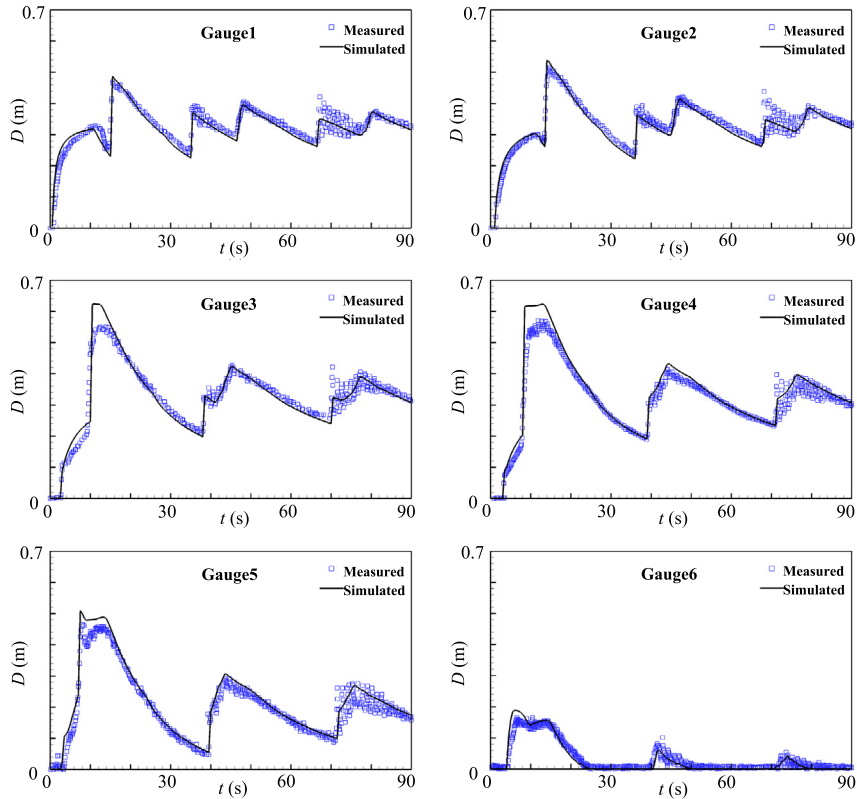
Fig. 11. Example 5: Computed and measured water depth as a function of time at different gauge points.
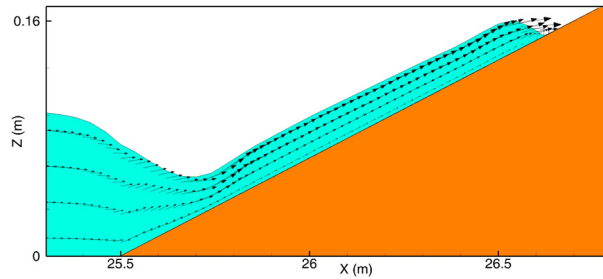

Fig. 12. Example 5: A cross-section at $y = 0$ of the water surface and velocity vector-field at time $t = 4$ when a wave runs up the hump.

5. Conclusion

In this paper, we have developed a new well-balanced and positivity preserving shock capturing numerical method for the 3-D SWEs. The contributions and conclusions of the present study are discussed below.

The main contribution of this paper is that we have applied a relaxation approach to the 3-D shallow water system and "hyperbolized" it. We then developed a well-balanced and positivity preserving second-order semi-discrete central-upwind scheme for the extended relaxation system. The resulting shock capturing numerical method is applicable to cases with sharp gradients arising in, for example, dam-break flows. This extends the applicability of the 3-D shallow water model in σ-coordinates.

We have ensured the well-balanced property of the proposed numerical method by extending the well-balanced discretization of the geometric source terms proposed in [10] for 2-D SWEs discretized on triangular grids, to the 3-D SWEs discretized on prismatic cells. Based on conducted numerical experiments, we draw the conclusion that the proposed well-balanced discretization can guarantee the balance between the numerical fluxes and bottom topography source terms and the well-balanced property can prevent the appearance of unphysical waves in the simulations of quasi-steady states. In addition, in order to maintain the stability in cells with very small water depth and preserve the positivity of water depth throughout the entire computational domain, a continuous piecewise linear reconstruction of the bottom topography and a positivity preserving reconstruction of the water surface are applied to guarantee that the resulting numerical method

is positivity preserving. The success in preserving the positivity of the water depth can also greatly extend the application range of the 3-D shallow water model.

The proposed relaxation based numerical method has been tested on five numerical experiments. The ability of our method to accurately compute sharp gradients has been demonstrated in Examples 1 and 5. The accuracy of the proposed numerical method is verified by comparing the computed results with analytical solutions or laboratory data; see Examples 1, 2 and 5. The importance of the well-balanced has been illustrated in Examples 3 and 4. The capability of the developed method to preserve the positive water depth have been demonstrated in Examples 4 and 5.

In summary, we have provided a novel framework for building 3-D shallow water systems, and thus their applicability range can be extended by adding other components, such as the Coriolis force, non-hydrostatic pressure and horizontal diffusion.

Acknowledgements

References

[1] R. Abgrall, S. Karni, Two-layer shallow water system: a relaxation approach, SIAM J. Sci. Comput. 31 (3) (2009) 1603–1627.
[2] C. Ai, S. Jin, B. Lv, A new fully non-hydrostatic 3D free surface flow model for water wave motions, Int. J. Numer. Methods Fluids 66 (11) (2011) 1354–1370.
[3] F. Alcrudo, P. Garcia-Navarro, A high-resolution Godunov-type scheme in finite volumes for the 2D shallow-water equations, Int. J. Numer. Methods Fluids 16 (6) (1993) 489–505.
[4] E. Audusse, F. Bouchut, M.-O. Bristeau, R. Klein, B. Perthame, A fast and stable well-balanced scheme with hydrostatic reconstruction for shallow water flows, SIAM J. Sci. Comput. 25 (6) (2004) 2050–2065.
[5] A. Beljadid, A. Mohammadian, A. Kurganov, Well-balanced positivity preserving cell-vertex central-upwind scheme for shallow water flows, Comput. Fluids 136 (2016) 193–206.
[6] A.F. Blumberg, G.L. Mellor, A coastal ocean numerical model, in: Mathematical Modelling of Estuarine Physics, Springer, 1980, pp. 203–219.
[7] A.F. Blumberg, G.L. Mellor, A description of a three-dimensional coastal ocean circulation model, in: Three-Dimensional Coastal Ocean Models, 1987, pp. 1–16.
[8] A. Bollermann, G. Chen, A. Kurganov, S. Noelle, A well-balanced reconstruction of wet/dry fronts for the shallow water equations, J. Sci. Comput. 56 (2) (2013) 267–290.
[9] W. Boscheri, M. Dumbser, M. Righetti, A semi-implicit scheme for 3D free surface flows with high-order velocity reconstruction on unstructured Voronoi meshes, Int. J. Numer. Methods Fluids 72 (6) (2013) 607–631.
[10] S. Bryson, Y. Epshteyn, A. Kurganov, G. Petrova, Well-balanced positivity preserving central-upwind scheme on triangular grids for the Saint–Venant system, Modél. Math. Anal. Numér. 45 (3) (2011) 423–446.
[11] V. Casulli, G.S. Stelling, Numerical simulation of 3D quasi-hydrostatic, free-surface flows, J. Hydraul. Eng. 124 (7) (1998) 678–686.
[12] V. Casulli, R.A. Walters, An unstructured grid, three-dimensional model based on the shallow water equations, Int. J. Numer. Methods Fluids 32 (3) (2000) 331–348.
[13] C. Chen, H. Liu, R.C. Beardsley, An unstructured grid, finite-volume, three-dimensional, primitive equations ocean model: application to coastal ocean and estuaries, J. Atmos. Ocean. Technol. 20 (1) (2003) 159–186.
[14] F. Coquel, K. El Amine, E. Godlewski, B. Perthame, P. Rascle, A numerical method using upwind schemes for the resolution of two-phase flows, J. Comput. Phys. 136 (1997) 272–288.
[15] O. Delestre, C. Lucas, P.A. Ksinant, F. Darboux, C. Laguerre, T.N. Vo, F. James, S. Cordier, et al., Swashes: a compilation of shallow water analytic solutions for hydraulic and environmental studies, Int. J. Numer. Methods Fluids 72 (3) (2013) 269–300.
[16] A.I. Delis, T. Katsaounis, Numerical solution of the two-dimensional shallow water equations by the application of relaxation methods, Appl. Math. Model. 29 (8) (2005) 754–783.
[17] M.I. Drago, L. Iovenitti, σ-Coordinates hydrodynamic numerical model for coastal and ocean three-dimensional circulation, Ocean Eng. 27 (10) (2000) 1065–1085.
[18] S. Gottlieb, D. Ketcheson, C.-W. Shu, Strong Stability Preserving Runge–Kutta and Multistep Time Discretizations, World Scientific Publishing Co. Pte. Ltd., Hackensack, NJ, 2011.
[19] S. Gottlieb, C.-W. Shu, E. Tadmor, Strong stability-preserving high-order time discretization methods, SIAM Rev. 43 (2001) 89–112.
[20] N. Goutal, F. Maurel, Proceedings of the second workshop on dam-break wave simulation, Technical report, Technical Report HE-43/97/016/A, Electricité de France, Département Laboratoire National d'Hydraulique, Groupe Hydraulique Fluviale, 1997.
[21] N.S. Heaps, Vertical structure of current in homogeneous and stratified waters, in: Hydrodynamics of Lakes, Springer, Vienna, 1984, pp. 153–207.
[22] J. Hou, F. Simons, M. Mahgoub, R. Hinkelmann, A robust well-balanced model on unstructured grids for shallow water flows with wetting and drying over complex topography, Comput. Methods Appl. Mech. Eng. 257 (2013) 126–149.
[23] P. Jawahar, H. Kamath, A high-resolution procedure for Euler and Navier–Stokes computations on unstructured grids, J. Comput. Phys. 164 (1) (2000) 165–203.
[24] M.B. Koçyigit, R.A. Falconer, Three-dimensional numerical modelling of wind-driven circulation in a homogeneous lake, Adv. Water Resour. 27 (12) (2004) 1167–1178.
[25] A. Kurganov, D. Levy, Central-upwind schemes for the Saint–Venant system, Modél. Math. Anal. Numér. 36 (2002) 397–425.
[26] A. Kurganov, C.-T. Lin, On the reduction of numerical dissipation in central-upwind schemes, Commun. Comput. Phys. 2 (2007) 141–163.
[27] A. Kurganov, S. Noelle, G. Petrova, Semi-discrete central-upwind scheme for hyperbolic conservation laws and Hamilton–Jacobi equations, SIAM J. Sci. Comput. 23 (2001) 707–740.
[28] A. Kurganov, G. Petrova, Central-upwind schemes on triangular grids for hyperbolic systems of conservation laws, Numer. Methods Partial Differ. Equ. 21 (3) (2005) 536–552.
[29] A. Kurganov, G. Petrova, A second-order well-balanced positivity preserving central-upwind scheme for the Saint-Venant system, Commun. Math. Sci. 5 (2007) 133–160.

[30] A. Kurganov, E. Tadmor, New high resolution central schemes for nonlinear conservation laws and convection–diffusion equations, J. Comput. Phys. 160 (2000) 241–282.
[31] A. Kurganov, E. Tadmor, Solution of two-dimensional Riemann problems for gas dynamics without Riemann problem solvers, Numer. Methods Partial Differ. Equ. 18 (2002) 584–608.
[32] R.J. LeVeque, Balancing source terms and flux gradients in high-resolution Godunov methods: the quasi-steady wave-propagation algorithm, J. Comput. Phys. 146 (1) (1998) 346–365.
[33] C.W. Li, B. Zhu, A sigma coordinate 3D k–ϵ model for turbulent free surface flow over a submerged structure, Appl. Math. Model. 26 (12) (2002) 1139–1150.
[34] Q. Liang, F. Marche, Numerical resolution of well-balanced shallow water equations with complex source terms, Adv. Water Resour. 32 (6) (2009) 873–884.
[35] P. Lin, A multiple-layer σ-coordinate model for simulation of wave–structure interaction, Comput. Fluids 35 (2) (2006) 147–167.
[36] P. Lin, C.W. Li, A σ-coordinate three-dimensional numerical model for surface wave propagation, Int. J. Numer. Methods Fluids 38 (11) (2002) 1045–1068.
[37] X. Liu, A. Mohammadian, A. Kurganov, J.A. Infante Sedano, Well-balanced central scheme for a fully coupled shallow water system modeling flows over erodible bed, J. Comput. Phys. 300 (2015) 202–218.
[38] G.I. Marchuk, Metody Rasshchepleniya, Nauka, Moscow, 1988 (Russian) [Splitting Methods].
[39] G.I. Marchuk, Splitting and alternating direction methods, in: Handbook of Numerical Analysis, vol. I, Handb. Numer. Anal., I, North-Holland, Amsterdam, 1990, pp. 197–462.
[40] A. Mohamadian, D.Y. Le Roux, M. Tajrishi, K. Mazaheri, A mass conservative scheme for simulating shallow flows over variable topographies using unstructured grid, Adv. Water Resour. 28 (5) (2005) 523–539.
[41] M. Morris, CADAM: Concerted Action on Dam Break Modelling—Final Report, HR Wallingford, Wallingford, 2000.
[42] H. Nessyahu, E. Tadmor, Nonoscillatory central differencing for hyperbolic conservation laws, J. Comput. Phys. 87 (2) (1990) 408–463.
[43] N.A. Phillips, A coordinate system having some special advantages for numerical forecasting, J. Meteor. 14 (2) (1957) 184–185.
[44] J. Pietrzak, J.B. Jakobson, H. Burchard, H. Jacob Vested, O. Petersen, A three-dimensional hydrostatic model for coastal and ocean modelling using a generalised topography following co-ordinate system, Ocean Model. 4 (2) (2002) 173–205.
[45] W. Rodi, Turbulence Models and Their Application in Hydraulics, CRC Press, 1993.
[46] P.L. Roe, Characteristic-based schemes for the Euler equations, Annu. Rev. Fluid Mech. 18 (1986) 337–365.
[47] R. Saurel, R. Abgrall, A multiphase Godunov method for compressible multifluid and multiphase flows, J. Comput. Phys. 150 (2) (1999) 425–467.
[48] H. Shirkhani, A. Mohammadian, O. Seidou, A. Kurganov, A well-balanced positivity-preserving central-upwind scheme for shallow water equations on unstructured quadrilateral grids, Comput. Fluids 126 (2016) 25–40.
[49] C.-W. Shu, S. Osher, Efficient implementation of essentially non-oscillatory shock-capturing schemes, J. Comput. Phys. 77 (2) (1988) 439–471.
[50] L. Song, J. Zhou, J. Guo, Q. Zou, Y. Liu, A robust well-balanced finite volume model for shallow water flows with wetting and drying over irregular terrain, Adv. Water Resour. 34 (7) (2011) 915–932.
[51] G. Stelling, M. Zijlema, An accurate and efficient finite-difference algorithm for non-hydrostatic free-surface flow with application to wave propagation, Int. J. Numer. Methods Fluids 43 (1) (2003) 1–23.
[52] G. Strang, On the construction and comparison of difference schemes, SIAM J. Numer. Anal. 5 (1968) 506–517.
[53] P.K. Sweby, High resolution schemes using flux limiters for hyperbolic conservation laws, SIAM J. Numer. Anal. 21 (5) (1984) 995–1011.
[54] B. Van Leer, Towards the ultimate conservative difference scheme. V. A second-order sequel to Godunov's method, J. Comput. Phys. 32 (1) (1979) 101–136.
[55] M.E. Vazquez-Cendon, Improved treatment of source terms in upwind schemes for the shallow water equations in channels with irregular geometry, J. Comput. Phys. 148 (1999) 497–526.
[56] J. Xia, R.A. Falconer, B. Lin, G. Tan, Modelling flood routing on initially dry beds with the refined treatment of wetting and drying, Int. J. River Basin Manag. 8 (3–4) (2010) 225–243.
[57] J.G. Zhou, D.M. Causon, C.G. Mingham, D.M. Ingram, The surface gradient method for the treatment of source terms in the shallow-water equations, J. Comput. Phys. 168 (1) (2001) 1–25.